

Final Draft
of the original manuscript:

Schuster, R.; Schafler, E.; Schell, N.; Kunz, M.; Abart, R.:

**Microstructure of calcite deformed by high-pressure torsion:
An X-ray line profile study**

In: Tectonophysics (2017) Elsevier

DOI: [10.1016/j.tecto.2017.10.015](https://doi.org/10.1016/j.tecto.2017.10.015)

Microstructure of calcite deformed by high-pressure torsion: an X-ray line profile study

Roman Schuster^a, Erhard Schafner^b, Norbert Schell^c, Martin Kunz^d, Rainer Abart^a

^a*University of Vienna, Department of Lithospheric Research, Althanstrasse 14, A-1090 Vienna, Austria*

^b*Research Group Physics of Nanostructured Materials, Faculty of Physics, University of Vienna, A-1090 Vienna, Austria*

^c*Institute of Materials Research, Helmholtz-Zentrum Geesthacht, Max-Planck-Strasse 1, D-21502 Geesthacht, Germany*

^d*Lawrence Berkeley National Laboratory, 1 Cyclotron Road, Berkeley, CA 94720, USA*

Abstract

Calcite aggregates were deformed to high strain using high-pressure torsion and applying confining pressures of 1-6 GPa and temperatures between room temperature and 450°C. The run products were characterized by X-ray diffraction, and key microstructural parameters were extracted employing X-ray line profile analysis. The dominant slip system was determined as $r\{10\bar{1}4\}\langle\bar{2}021\rangle$ with edge dislocation character. The resulting dislocation density and the size of the coherently scattering domains (CSD) exhibit a systematic dependence on the P - T conditions of deformation. While high pressure generally impedes recovery through reducing point defect mobility, the picture is complicated by pressure-induced phase transformations in the CaCO_3 system. Transition from the calcite stability field to those of the high-pressure polymorphs CaCO_3 -II, CaCO_3 -III and CaCO_3 -IIIb leads to a change of the microstructural evolution with deformation. At 450°C and pressures within the calcite stability field, dislocation densities and CSD sizes saturate at shear strains exceeding 10 in agreement with earlier studies at lower pressures. In the stability field of CaCO_3 -II, the dislocation density exhibits a more complex behavior. Furthermore, at a given strain and strain rate, the dislocation density increases and the CSD size decreases with increasing pressure within the stability fields of either calcite or of the high-pressure polymorphs. There is, however, a jump from high dislocation densities and small CSDs in the upper pressure region of the calcite stability field to lower dislocation densities and larger CSDs in the low-pressure region of the CaCO_3 -II stability field. This jump is more pronounced at higher temperatures and less so at room temperature. The pressure influence on the deformation-induced evolution of dislocation

densities implies that pressure variations may change the rheology of carbonate rocks. In particular, a weakening is expected to occur at the transition from the calcite to the CaCO_3 -II stability field, if aragonite does not form.

1. Introduction

Calcite is an important rock-forming mineral in the earth's crust, and it plays a key role in the earth's carbon cycle. Due to the relative weakness of calcite compared to other common rock-forming minerals, strain localization and formation of shear zones often occur in calcite-bearing rocks (van der Pluijm, 1991; Romeo et al., 2007; Fernández et al., 2004). Carbonate rocks may undergo ductile deformation at relatively low temperatures and high pressures, as may prevail in old continental lithospheres with low geothermal gradients and may be generated by tectonic overpressure (Peacock and Wang, 1999; Warren, 2013; Vrijmoed et al., 2009; Gerya et al., 2008; Li et al., 2010). In this context, the deformation behavior of calcite at relatively low temperatures and high confining pressures in the GPa range is of central interest.

Experimental rock deformation has provided key information on the conditions and mechanisms of rock deformation in natural systems. Deformation experiments and studies on naturally deformed rocks are tied together by the resulting microstructures (Herwegh et al., 2005). Calcite-bearing rocks are among the most intensely studied rock types both in natural settings (e.g. (Bestmann and Prior, 2003; Burkhard, 1993)) as well as in laboratory experiments (e.g. (De Bresser et al., 2002; Renner et al., 2002)). Initially, deformation experiments on calcite were limited to tensile, compression and triaxial tests (Turner et al., 1954; Griggs et al., 1960; De Bresser and Spiers, 1997) or torsional deformation to comparatively low strains (Handin et al., 1960) or under poorly constrained conditions (Bridgman, 1936). Natural rock deformation is often localized in shear zones where non-coaxial deformation to high strain occurs. Experimental rock deformation must therefore also explore the high-strain case.

Torsion experiments are ideally suited for investigating non-coaxial deformation to high strain. The Paterson deformation apparatus has been the standard device for torsional deformation experiments on geological materials (Paterson and Olgaard, 2000). This apparatus allows for torsional deformation to high strains at temperatures up to 1300°C and confining pressures up to 500 MPa. Experiments have been designed using the Paterson apparatus to study the relations between stress and strain-rate, deforma-

tion induced microstructure evolution, as well as dynamic and static recrystallization of calcite aggregates at P - T conditions prevailing in the earth's crust (Casey et al., 1998; Paterson and Olgaard, 2000; Pieri et al., 2001a,b; Barnhoorn et al., 2004, 2005).

The potential influence of confining pressures in the GPa range on deformation and related microstructures is, however, out of reach with the Paterson apparatus. Nevertheless, deformation of CaCO_3 at high confining pressures in the GPa range is particularly interesting. Apart from several CaCO_3 polymorphs that are stable or metastable at ambient conditions (calcite, aragonite and vaterite) a number of high-pressure polymorphs exist, which form, when calcite is subjected to pressures in the GPa range (Bridgman, 1938; Merrill and Bassett, 1975; Merlini et al., 2012; Fiquet et al., 1994). At room temperature trigonal calcite transforms to CaCO_3 -II at 1.7 GPa and further to CaCO_3 -IIIb at 1.9 GPa and to CaCO_3 -III at 3.3 GPa. The crystal structure of the CaCO_3 -II polymorph was determined as a monoclinic structure with space group $P2_1/c$ (Merrill and Bassett, 1975) and a density of 2.77 g cm^{-3} compared to a density of 2.71 g cm^{-3} for calcite at ambient conditions. The crystal structures of CaCO_3 -III and CaCO_3 -IIIb were determined by Merlini et al. (2012) to be triclinic with space group P1. The densities of these phases are 2.99 g cm^{-3} for CaCO_3 -III at a pressure of 2.8 GPa and 2.96 g cm^{-3} for CaCO_3 -IIIb at a pressure of 3.1 GPa, which is still lower than the density of aragonite indicating that these phases are not the thermodynamically stable phases in this pressure range (Merrill and Bassett, 1975). Recently Schaebitz et al. (2015) have reported the occurrence of CaCO_3 -III and CaCO_3 -IIIb nanocrystals in natural rocks that had been deformed during a land-slide event. The mechanisms of non-coaxial deformation of CaCO_3 at confining pressures in the GPa range and the resulting microstructures and textures are not known. In particular, the potential influence of high confining pressure on the activation of slip systems and intracrystalline deformation as well as on recovery and recrystallization is of key interest.

At the moderate temperatures that are relevant for this study, intracrystalline plastic deformation in calcite proceeds mainly by mechanical twinning, dislocation glide, climb, and cross slip. Figure 1 shows the commonly observed twinning and slip systems in calcite. Throughout this study we utilize the 4-index Miller Bravais indexation for the hexagonal unit cell of calcite, except for the notation of Bragg reflexions, where we omit the third index. Studies of experimentally and naturally deformed calcite have revealed three different deformation twinning systems, namely twinning on $e\{01\bar{1}8\}$ -, $r\{10\bar{1}4\}$ - and

$f\{01\bar{1}2\}$ planes. The slip systems show three sets of Burgers vectors namely $1/3\langle\bar{2}021\rangle$, $1/3\langle10\bar{1}1\rangle$ and $1/3\langle2\bar{1}\bar{1}0\rangle$. Possible slip planes are the rhombohedral planes $r\{10\bar{1}4\}$ and $f\{01\bar{1}2\}$, the prismatic planes $a\{\bar{1}2\bar{1}0\}$ and $m\{10\bar{1}0\}$ as well as the basal plane $c(0001)$.

In this study we present results from experimental high-strain torsional deformation of CaCO_3 at pressures in the GPa range. To this end, high-pressure torsion (HPT), a deformation method routinely used in materials science for producing bulk nanostructured materials, was used. In HPT a special anvil geometry provides quasi-hydrostatic pressure conditions in the GPa range in the sample during torsional deformation (Zhilyaev and Langdon, 2008).

For investigating the microstructures resulting from the HPT experiments X-ray line profile analysis (XPA) was employed. This technique uses the broadening of Bragg reflections due to deviations of atomic positions in real crystals from their sites in the ideal lattice. In this study we analyzed the peak broadening due to lattice strain caused by dislocations to determine dislocation densities and the active slip systems. In addition, the peak broadening resulting from the finite extent of the coherently scattering domains (CSD) was used to determine the evolution of the CSD size during HPT deformation. The X-ray diffraction profiles of samples deformed at temperatures between room temperature and 450°C under confining pressures ranging from 1 GPa to 6 GPa to different strains and at different strain rates were analyzed.

2. X-ray Line Profile analysis

The 2D powder pattern of an ideal crystal is given by delta-function shaped diffraction peaks the positions of which are determined by the crystal structure. In contrast, the peaks of powder patterns of real lattices may be shifted from their ideal position, symmetrically or asymmetrically broadened or deviate in some other manner from the ideal peak shape (Warren and Averbach, 1952). These deviations of the X-ray diffraction patterns of real crystals from the patterns of ideal crystals are due to the displacement of atom positions in the real lattice from the corresponding atom positions in an ideal lattice as well as due to the finite size of the crystallites (Warren and Averbach, 1952; Williamson and Hall, 1953). Atomic displacements or lattice strain may be caused by zero-, one-, or two-dimensional lattice defects, which influence diffraction patterns in specific manners (Krivoglaz, 1969).

In X-ray Line Profile analysis (XPA) the deviations of the Bragg peaks from their

Slip systems:

$a\{\bar{1}2\bar{1}0\}\langle\bar{2}021\rangle$
 $c\{0001\}\langle\bar{1}2\bar{1}0\rangle$
 $f\{\bar{1}0\bar{1}2\}\langle\bar{2}\bar{2}01\rangle$
 $f\{\bar{1}0\bar{1}2\}\langle 10\bar{1}1\rangle$
 $m\{10\bar{1}0\}\langle\bar{1}2\bar{1}0\rangle$
 $r\{10\bar{1}4\}\langle\bar{1}2\bar{1}0\rangle$
 $r\{10\bar{1}4\}\langle\bar{2}021\rangle$

Twin systems:

$180^\circ/e\{\bar{1}0\bar{1}8\}$
 $180^\circ/r\{10\bar{1}4\}$
 $180^\circ/f\{\bar{1}0\bar{1}2\}$

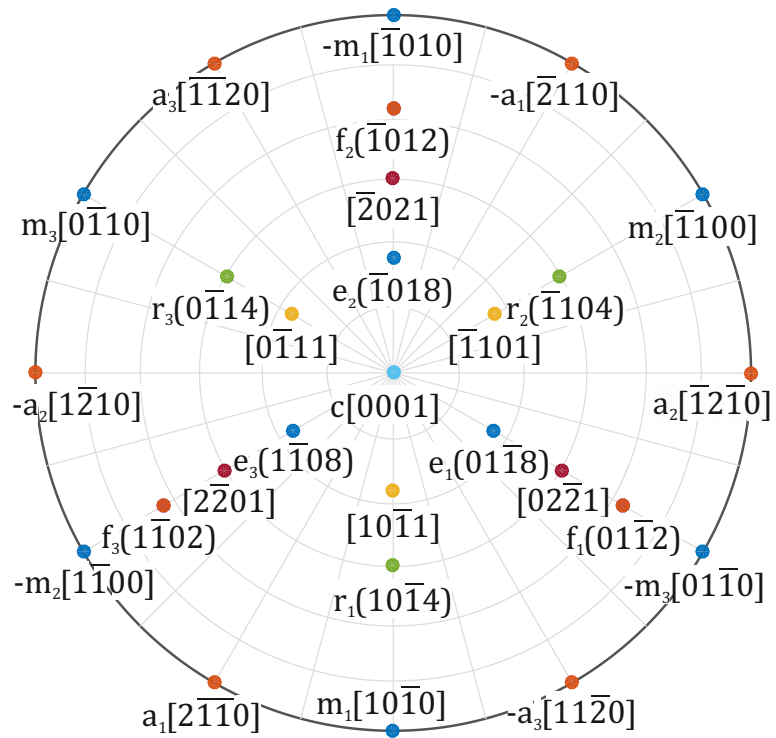


Figure 1: Stereographic projection of calcite marked with the plane poles and directions relevant for slip and twinning. Due to the trigonal symmetry of calcite the orientations of plane poles and directions with the same Miller-Bravais indices in the basal plane and normal to it are equivalent and noted as directions in this plot. The grid spacing is 15° . In addition, the known slip and deformation twinning systems in calcite are listed.

ideal shape and position are used to extract information on the nature and quantity of defects in the crystal lattice as well as on the size and shape of the crystallites. XPA is complementary to electron microscopy, since it samples larger areas on the surface and, depending on the wavelength of the X-ray beam applied, it also probes deeper into the sample. This ensures better statistical reliability compared to microstructure analysis based on scanning electron microscopy (SEM) and especially transmission electron microscopy (TEM). Moreover, XPA can be used for in-situ investigations at P - T conditions that may not be replicated in an SEM or TEM. Furthermore, XPA is suitable for the study of very high dislocation densities or beam sensitive materials which cannot be analyzed by TEM.

2.1. Theory

According to the kinematical theory of X-ray diffraction the intensity of the physical profile of a Bragg reflection I^P is given by the convolution of the intensities of the profile due to the finite size of the scattering domains I^S with the profile due to lattice strain I^D (Warren and Averbach, 1952).

$$I^P = I^S * I^D \quad (1)$$

In Fourier space it is therefore possible to separate the broadening caused by size and strain giving rise to the Warren-Averbach equation (Warren and Averbach, 1952):

$$\ln A^P(L) = \ln A^S(L) + \ln A^D(L), \quad (2)$$

where A^P , A^S and A^D are the Fourier coefficients of the physical profile, the size Fourier coefficients and the strain or distortion Fourier coefficients, and L is the Fourier length. The size Fourier coefficients depend on the extension of the coherently scattering domain (CSD) along the diffraction vector. In the absence of shape preferred orientation, it is independent of diffraction order. In contrast, the strain broadening coefficients as calculated by Warren and Averbach depend on diffraction order (Warren and Averbach, 1952)

$$A^D(L) = \exp[-2\pi^2 L^2 g^2 \langle \epsilon_{g,l}^2 \rangle], \quad (3)$$

where g is the absolute value of the diffraction vector and $\langle \epsilon_{g,l}^2 \rangle$ is the mean square strain. It is therefore possible to distinguish between peak broadening caused by the finite size

of the CSD and the broadening caused by lattice strain. For the case, where the lattice distortion is caused by dislocations, $\langle \epsilon_{g,l}^2 \rangle$ was calculated by Wilkens (1970)

$$\langle \epsilon_{g,l}^2 \rangle \approx \frac{\rho C b^2}{4\pi} f(L/R_e), \quad (4)$$

where ρ is the dislocation density, b is the length of the Burgers vector of the active slip system, and C is the dislocation contrast factor. The contrast factor accounts for the different degrees of “visibility“ of the strain field caused by different dislocations. It is determined by the elastic properties of the material and the relative orientations of the line and Burgers vector of the dislocation and the diffraction vector. The Wilkens function $f(L/R_e)$, the explicit form of which is given in Wilkens (1970), describes the strain field caused by the dislocation for the dislocation arrangement assumed by Wilkens. The outer cut off radius R_e , describing the range of the strain field, varies according to the configuration of the dislocations, which may lead to a partial screening of their strain fields.

2.2. Strain anisotropy

When lattice strain is caused by dislocations, the strain broadening of Bragg reflections increases with the magnitude of the diffraction vector as can be seen in Eq. 3, but it also depends on the orientation of the diffraction vector. The anisotropy in strain broadening is due to the anisotropic nature of the strain fields associated with dislocations. This implies that, similarly to dislocation contrast in TEM, the dislocation contrast changes with varying orientation of the diffraction vector relative to the dislocation. In particular, the dislocation contrast depends on the anisotropy of the elastic properties of the crystal, and for non-cubic crystals it also depends on the respective ratios of the lattice parameters and the angles between the crystal directions. Furthermore, it depends on the orientations of the line- and Burgers vectors of the dislocation and on the orientation of the diffraction vector.

In polycrystals with no or weak texture, slip systems with symmetrically equivalent slip planes and directions are activated to a similar extent. In this case the respective contrast factors may be averaged to obtain the averaged contrast factors \bar{C} of each set of equivalent slip systems. For crystals with hexagonal symmetry the averaged contrast factors can be parametrized as (Dragomir and Ungár, 2002; Ungár et al., 2001)

$$\bar{C} = \bar{C}_{hk0}(1 + q_1 x + q_2 x^2), \quad (5)$$

where \overline{C}_{hk0} is the averaged contrast factor of hk0 type reflections, $x = 2/3(l/ga)^2$, q_1 and q_2 are parameters depending on the lattice parameters, elastic constants and the active slip systems, l is the Miller index in the direction perpendicular to the basal plane, and a is the basal lattice parameter. This form allows to fit the dislocation contrast to the broadening of several Bragg reflections of an X-ray diffraction profile. The resulting experimental contrast factors can then be compared to the contrast factors calculated for the possible slip systems. Through this procedure the dominant slip system or the combination of active slip systems can be identified.

2.3. Whole Profile fitting

In whole profile fitting a diffraction pattern is simulated by using physical models that describe both size and strain broadening and incorporate the measured instrumental broadening (Ungár, 2004). The simulated patterns are then fitted to the measured diffraction profiles. In this study the whole profile fitting method was applied. To this end, we used the CMWP-fit software developed by Ribárik et al. (2001, 2004) and Ribárik (2008). In the CMWP-fit software size broadening is accounted for by assuming a log-normal distribution of the CSD-size and either spherical or ellipsoidal CSD shape. The probability density function of this distribution is given as

$$f(x) = \frac{1}{\sqrt{2\pi}\sigma x} \exp \left[-\frac{(\log(x/m))^2}{2\sigma^2} \right]. \quad (6)$$

For spherically shaped crystallites the size broadening is therefore described by the parameters m and σ . The m parameter is the scale parameter and median of the lognormal distribution, whereas σ is its shape parameter. For modeling the strain induced broadening the expression for the mean square strain in Eq. (4) is used. The fitting parameters, that are adjusted to construct the strain portion of the simulated diffraction pattern, are the dislocation density ρ , the effective outer cut-off radius R_e as well as the q_1 and q_2 parameters. Eq. (5) was used to account for strain anisotropy.

3. Experimental

3.1. Sample preparation

The starting material was prepared from a block of highly pure Carrara marble, which was crushed and sieved to a particle size of 63 - 100 μm . The powder was dried and then compacted into cylindrical pellets with 8 or 10 mm diameter at room temperature using

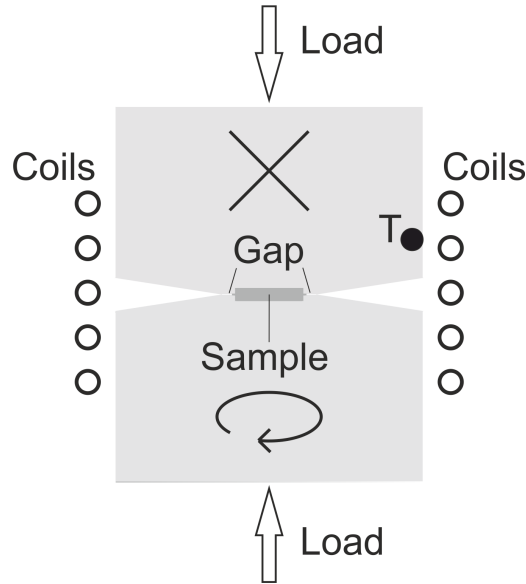


Figure 2: Schematic cross-section of an HPT assembly; the cylindrical sample is placed in the cavity between two anvils. The top anvil is fixed after the pressure is applied while the bottom anvil is rotated. The sample confinement is provided by sample material, which flows into the narrow gap between the two anvils and hardens at the onset of the torsion deformation thereby providing the necessary back-pressure for the quasi-hydrostatic pressure conditions. The temperature regulation is managed by a controller, which is coupled with the induction furnace and a pyrometer focused on point (T) on the upper anvil. The induction coils extend about 2 cm above and below the sample. The HPT apparatus is held at room temperature by water cooling about 10 cm above and below the sample, ensuring well-constrained temperature conditions during deformation.

a cold press. The amount of powder was chosen as to obtain a pellet with 0.8 mm thickness assuming zero porosity. The pre-pressed powder samples show a weak texture with a preferred orientation of the c -axes parallel to the compaction direction i.e. normal to the basal plane of the cylindrical sample. The a -axes of the crystallites that have their c -axis aligned with the compaction direction are randomly orientated within the basal plane of the cylindrical pellet.

3.2. High Pressure Torsion

A high pressure torsion (HPT) apparatus at the Faculty of Physics, University of Vienna was used for the torsion experiments. During HPT deformation cylindrical samples are subjected to quasi-hydrostatic pressure of several GPa in addition to concurrent torsional deformation (Zhilyaev and Langdon, 2008). Quasi-hydrostatic-pressure is fa-

cilitated by the geometry of the pressure anvils. Both anvils contain a cylindrical cavity with the same diameter as the sample into which the samples are fitted (see Fig. 2). The combined depth of the two cavities is slightly smaller than the initial sample height, leaving a gap of about 100 μm between the anvils. At the onset of a deformation experiment sample material flows into the gap between the anvils, where it hardens due to friction thereby providing the back pressure necessary for the quasi-hydrostatic pressure conditions (Vorhauer and Pippan, 2004). This provides homogeneous pressure conditions for the specimen except for the very rim of the sample, which was not analyzed in this study (Lee et al., 2014). The quasi-hydrostatic-pressure conditions permit deformation experiments to arbitrarily high strain, while the sample geometry is largely retained.

The HPT machine used allows to deform cylindrical samples of up to 10 mm diameter and 0.8 mm height at pressures from about 1 GPa up to 8 GPa. Deformation at elevated temperatures up to about 450°C is facilitated by induction heating of the HPT-anvils (see Fig. 2). The temperature was measured with a pyrometer coupled to the heating control regulating the power output of the induction coils. The pyrometer was focused on the surface of the upper anvil 2 mm above the sample. Given the slow angular velocity of 0.02 rotations per minute (RPM) during HPT-processing, a possible temperature increase in the sample due to deformation heating is negligible (Figueiredo et al., 2012). Similarly, the small sample thickness and the high heat capacity of the anvils ensure a uniform temperature distribution. To check for possible slippage between sample and anvils during HPT-deformation, test runs were performed at various $P - T$ conditions, where marks were applied along the sample radius on the bottom and top surfaces before deformation. All tests showed that no slippage occurred and that the specified torsion was completed along the entire radius. The local shear strain γ in the sample after deformation is given by

$$\gamma = \frac{2\pi nr}{t}, \quad (7)$$

where n is the number of rotations, r is the distance from the rotation axis, and t is the thickness of the sample. The equivalent von Mises strain ϵ is then calculated as

$$\epsilon = \frac{\gamma}{\sqrt{3}}. \quad (8)$$

Samples were deformed at room temperature, 235°C and 450°C at pressures between 1 and 6 GPa. The sample diameter was 10 mm for samples deformed at 1 GPa and 8 mm for samples deformed under higher confining pressures. The sample thickness

post-deformation was 0.6 mm for all samples. All samples were deformed at a constant twist rate of 0.02 RPM, which corresponds to a maximum equivalent strain rate of about $1 \times 10^{-2} \text{ s}^{-1}$ at the edge of a sample with 10 mm diameter and of about $8 \times 10^{-3} \text{ s}^{-1}$ at the edge of a sample with 8 mm diameter. After deformation at elevated temperatures the samples were cooled under pressure to 50°C before the pressure was released. Observation by light-optical microscopy and SEM showed no porosity in the samples post-deformation regardless of the deformation temperature.

3.3. X-ray diffraction experiments

High-quality X-ray diffraction patterns were obtained from diffraction experiments performed at the P07-HEMS beamline at PETRA III, Deutsches Elektronen-Synchrotron (DESY, Hamburg) (Schell et al., 2014) using a monochromatic X-ray beam with an energy of 50 keV. The diffraction experiments were carried out in transmission geometry parallel to the rotation axis with a spot size of 500 μm by 200 μm . The measurements were taken every 500 μm from the center to the rim along a radial profile normal to the rotation axis. The diffractograms were recorded with a 2D Perkin Elmer XRD 1621 detector.

Additional measurements were carried out at the Microdiffraction beamline at the Advanced Light Source, Lawrence Berkeley National Laboratory, Berkeley, USA. In contrast to the measurements at DESY the ALS measurements were performed in reflection geometry with a monochromatic beam of 12 keV energy and 30 μm spot size on the sample, where, similarly to the experiments at DESY, profiles along the sample radius were measured. The diffractograms were recorded with a 2D Pilatus 1M detector. For all measurements the resulting Debye-Scherrer rings were then azimuthally integrated with the Fit2D software (Hammersley, 1997; Hammersley et al., 1996) to obtain diffraction patterns.

Due to the relatively large footprint of the beam at the DESY beamline, the measurements sampled over relatively large radial distances and thus incorporated a range of strains and strain rates. This effect is particularly pronounced for measurements close to the sample center. Assuming that the beam is placed exactly on the center of a sample deformed for one rotation at 0.02 RPM, the von Mises equivalent strain ϵ in the illuminated region ranges from 0 to 1.5 with an average of 0.8. The von Mises equivalent strain rate $\dot{\epsilon}$ ranges from 0 to $5.1 \times 10^{-4} \text{ s}^{-1}$ with an average of $2.6 \times 10^{-4} \text{ s}^{-1}$. Due to the comparatively small footprint of the beam at ALS, ϵ varies from 0 to 0.2 and $\dot{\epsilon}$ from 0

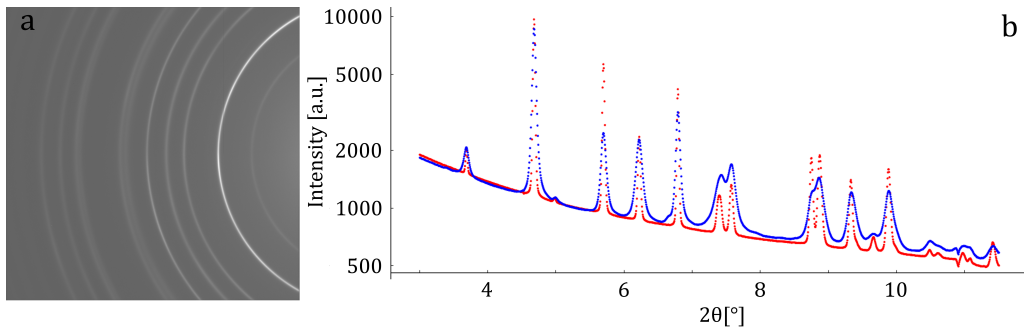


Figure 3: X-ray diffraction data. (a) raw data from the 2D Perkin Elmer XRD 1621 detector at DESY of a sample deformed at 2 GPa at room temperature taken 3 mm from the rotation axis. (b) integrated diffractograms of the raw data from (a) in blue as well as from a sample deformed under 2 GPa at 450°C taken 3 mm from the rotation axis, in red.

to $6.1 \times 10^{-5} \text{ s}^{-1}$ over the sampled area. On the other hand, the large illuminated volume of the DESY measurements ensures better statistical reliability than the smaller footprint of the ALS measurements. Table 1 lists the samples that were measured at DESY and ALS. Figure 3 shows a typical readout of the 2D detector at DESY as well as two diffractograms resulting from integration of the raw data with Fit2D. The diffractograms show the qualitative difference in the peak broadening of two samples deformed at room temperature and at 450°C applying the same confining pressure of 2 GPa, shear strain of $\gamma = 31$, and shear strain rate of $1 \times 10^{-2} \text{ s}^{-1}$. The diffractograms show significantly more pronounced peak broadening resulting from higher defect densities in samples deformed at room temperature than at 450°C.

3.4. Evaluation

The positions and intensities of the Bragg reflections were determined with the software “Fityk” (Wojdyr, 2010). For the XPA processing of the line profiles the CMWP-fit software and the software “multi_eval” (Kerber et al., 2009), which allows to vary the set of starting values for the fit parameters in CMWP-fit, were used. Stacking faults and twinning were not included in the evaluation. Peak broadening due to the presence of twins depends on the frequency of twin boundaries. For peak broadening due to twinning to be detectable by XPA in the presence of other defects, a twin boundary density of more than about 0.05 % would be required (Ungár et al., 2008). Considering *e*-twinning in calcite, this would correspond to a mean spacing of less than 400 nm between the twin

Table 1: Samples measured at DESY and ALS. The column 'Phase' indicates the stability fields of the CaCO_3 polymorphs corresponding to the $P - T$ conditions during deformation (Kondo et al., 1972; Pippinger et al., 2015), where calcite is denoted as phase I.

Sample name	Temperature	Pressure	Rotations	Phase	Beamline
rt-1.4-1	RT	1.4	1	I	DESY
rt-2-1	RT	2	1	IIIb	DESY
rt-4-1	RT	4	1	III	DESY
rt-4-2	RT	4	2	III	DESY
450-1.4-1	450°C	1.4	1	I	DESY
450-2-1	450°C	2	1	II	DESY
450-4-1/12	450°C	4	1/12	II	DESY
450-4-1	450°C	4	1	II	DESY
235-1-1	235°C	1	1	I	ALS
235-2-1	235°C	2	1	II	ALS
235-2-2	235°C	2	2	II	ALS
235-3-1	235°C	3	1	III	ALS
235-4-1	235°C	4	1	III	ALS
235-4-2	235°C	4	2	III	ALS
235-6-1	235°C	6	1	III	ALS
450-1-1	450°C	1	1	I	ALS
450-2-2	450°C	2	2	II	ALS
450-3-1	450°C	3	1	II	ALS

boundaries. SEM measurements showed that even after deformation at room temperature the twin boundary densities are much lower and therefore in our samples the Bragg peak broadening due to twinning is not resolvable by XPA. Instrumental broadening was incorporated into the evaluation by measuring the widths of Bragg peaks in the relevant 2θ range of unstrained standard samples at both beamlines.

While the CMWP-fit evaluation of most patterns gave values of about 10 nm for the outer cut-off radius, in some cases the evaluation resulted in unrealistic values for the outer cut-off radius and therefore unreliable dislocation densities. To ensure the comparability of the dislocation densities across all diffraction patterns, the outer cut-off

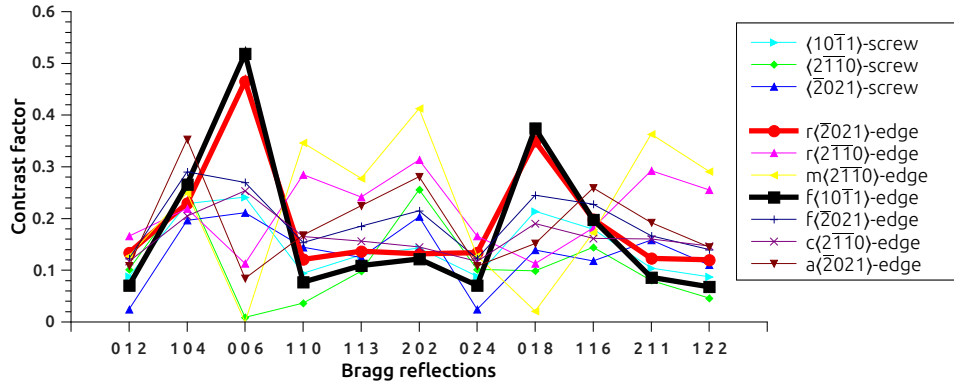


Figure 4: Theoretically calculated contrast factors for slip systems in calcite for edge (e) and screw (s) dislocations (see Table 2). The $r\{10\bar{1}4\}\langle \bar{2}021 \rangle$ -edge and $f\{\bar{1}012\}\langle 10\bar{1}1 \rangle$ -edge slip systems are shown as heavy symbols to highlight their similarity.

radius was fixed to 10 nm for all CMWP-fit evaluations.

The contrast factors for the slip systems observed in naturally and experimentally deformed calcite (Bestmann and Prior, 2003; De Bresser and Spiers, 1997; Pieri et al., 2001a) were calculated using the GNU Octave script “contrastfactor” written by Spieckermann (2010) on the basis of the work of Martinez-Garcia et al. (2009) for pure edge and screw dislocation character. The dislocation contrast factors for arbitrary crystal symmetries and Bragg reflections can be calculated with this script using the compliance or stiffness matrix and lattice parameters of the investigated material as well as the slip planes and Burgers vectors of the relevant slip systems as input.

The lattice parameters of calcite at room temperature and 1 bar atmospheric pressure were taken as 4.99 Å for the a parameter and 17.06 Å for the c parameter (Antao et al., 2009). The stiffness matrix of calcite at room temperature and 1 bar atmospheric pressure was taken from (Dandekar, 1968).

4. Results

The measured diffractograms do not show any reflections pertaining to aragonite or another calcium-carbonate polymorph other than calcite demonstrating that, if high pressure polymorphs were present during the HPT experiments, they were not preserved in the quenched samples.

Table 2: Theoretical contrast factors for the known slip systems as given in (De Bresser and Spiers, 1997) and the $r\{10\bar{1}4\}\langle\bar{1}2\bar{1}0\rangle$ slip system proposed in (Pieri et al., 2001b) for the first 11 Bragg reflections in calcite for pure edge (e) and screw (s) dislocations

Slip system	0 1 2	1 0 4	0 0 6	1 1 0	1 1 3	2 0 2	0 2 4	0 1 8	1 1 6	2 1 1	1 2 2
$a\{\bar{1}2\bar{1}0\}\langle\bar{2}021\rangle_e$	0.142	0.107	0.392	0.354	0.207	0.322	0.142	0.320	0.131	0.355	0.252
$c(0001)\langle\bar{1}2\bar{1}0\rangle_e$	0.142	0.246	0.217	0.193	0.196	0.233	0.142	0.198	0.202	0.202	0.177
$f\{\bar{1}012\}\langle\bar{2}201\rangle_e$	0.123	0.290	0.270	0.154	0.185	0.215	0.123	0.245	0.228	0.167	0.140
$f\{\bar{1}012\}\langle 10\bar{1}1\rangle_e$	0.071	0.266	0.519	0.077	0.109	0.122	0.071	0.374	0.198	0.086	0.068
$m\{10\bar{1}0\}\langle\bar{1}2\bar{1}0\rangle_e$	0.128	0.250	0.000	0.346	0.278	0.413	0.128	0.021	0.173	0.363	0.291
$r\{10\bar{1}4\}\langle\bar{2}021\rangle_e$	0.134	0.229	0.466	0.121	0.137	0.132	0.134	0.349	0.199	0.123	0.120
$r\{10\bar{1}4\}\langle\bar{1}2\bar{1}0\rangle_e$	0.166	0.219	0.113	0.285	0.242	0.313	0.166	0.113	0.182	0.293	0.255
$\langle\bar{2}\bar{1}\bar{1}0\rangle_s$	0.089	0.280	0.000	0.132	0.184	0.227	0.089	0.086	0.207	0.152	0.115
$\langle\bar{2}021\rangle_s$	0.235	0.663	0.139	0.379	0.546	0.646	0.235	0.207	0.524	0.481	0.391
$\langle 10\bar{1}1\rangle_s$	0.071	0.266	0.519	0.077	0.109	0.122	0.071	0.374	0.198	0.086	0.068

4.1. Slip system analysis

The contrast factors for the 012, 104, 006, 110, 113, 202, 024, 018, 116, 211 and 122 Bragg reflections were calculated for the $c(0001)\langle\bar{1}2\bar{1}0\rangle$, $r\{10\bar{1}4\}\langle\bar{1}2\bar{1}0\rangle$, $r\{10\bar{1}4\}\langle\bar{2}021\rangle$, $f\{\bar{1}012\}\langle\bar{2}201\rangle$, $f\{\bar{1}012\}\langle 10\bar{1}1\rangle$, $a\{\bar{1}2\bar{1}0\}\langle\bar{2}021\rangle$ and $m\{10\bar{1}0\}\langle\bar{1}2\bar{1}0\rangle$ slip systems for both pure edge and pure screw dislocation character with the aforementioned script “contrastfactor”. The contrast factors of the individual slip systems were then averaged assuming identical activity of each individual slip system belonging to one particular set of equivalent slip systems. For example, in the case of the $r\{10\bar{1}4\}\langle\bar{1}2\bar{1}0\rangle$ slip system the contrast factors of the individual Bragg reflections for the three equivalent slip systems $r(10\bar{1}4)[\bar{1}2\bar{1}0]$, $r(1\bar{1}0\bar{4})[\bar{1}\bar{1}20]$ and $r(0\bar{1}14)[2\bar{1}\bar{1}0]$ were averaged to compute the averaged contrast factors \bar{C} for the $r\{10\bar{1}4\}\langle\bar{1}2\bar{1}0\rangle$ set of slip systems. Table 2 lists the averaged contrast factors for the first eleven Bragg reflections for the known slip systems in calcite for both pure edge and pure screw character as given in (De Bresser and Spiers, 1997) and the $r\{10\bar{1}4\}\langle\bar{1}2\bar{1}0\rangle$ slip system proposed in (Pieri et al., 2001b).

The active slip systems were determined by comparing the theoretical contrast factors with the dislocation contrast extracted from the measured line profiles. Equation (5) was

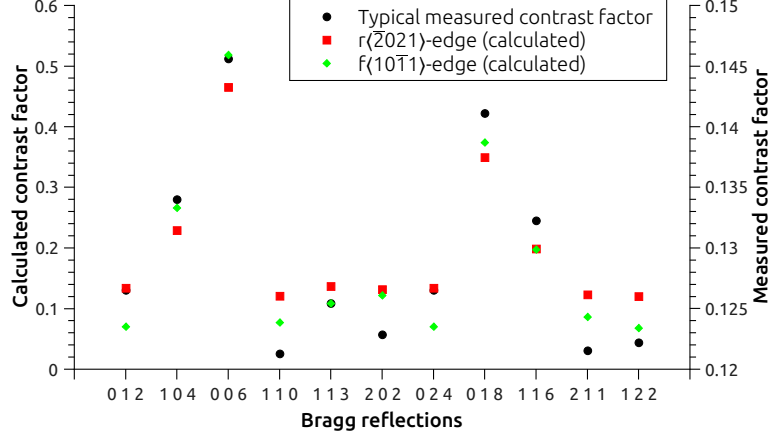


Figure 5: Experimentally determined contrast factors (right axis) and calculated contrast factors for the $r\{10\bar{1}4\}\langle\bar{2}021\rangle$ and $f\{\bar{1}012\}\langle10\bar{1}1\rangle$ slip systems for edge dislocations (left axis). The experimentally determined contrast factors show the same strain anisotropy as the two slip systems but with diminished extent.

used to obtain the contrast factors of the individual Bragg reflections from the fitting parameters q_1 and q_2 .

The comparison of the experimentally determined and the theoretically calculated contrast factors shown in Figures 5 and 4, respectively, reveals that only the edge dislocations of the $r\{10\bar{1}4\}\langle\bar{2}021\rangle$ slip system and of the $f\{\bar{1}012\}\langle10\bar{1}1\rangle$ slip system exhibit a similar anisotropy as the measured contrast factors. Even though the difference in the dislocation contrast of these two slip systems is too small to reliably distinguish between them (see Fig. 4), earlier studies on the deformation behavior of calcite have shown that for strain rates relevant to this study and deformation temperatures up to about 500°C the $f\{\bar{1}012\}\langle10\bar{1}1\rangle$ slip system is very unlikely to play a major role, whereas the $r\{10\bar{1}4\}\langle\bar{2}021\rangle$ slip system is dominant (De Bresser and Spiers, 1997). Thus, from our slip system analysis we infer that, apart from twinning on the $e\{10\bar{1}8\}$ and $r\{10\bar{1}4\}$ lattice planes, $r\{10\bar{1}4\}\langle\bar{2}021\rangle$ creep is the dominant mechanism of plastic deformation in our experiments. From the characteristic anisotropic broadening, the other low temperature slip system $f\{\bar{1}012\}\langle2\bar{2}01\rangle$ can be excluded (see Fig. 4). For the $r\{10\bar{1}4\}\langle\bar{2}021\rangle$ slip system there is very good qualitative correspondence in the anisotropy of the theoretically calculated and the experimentally determined contrast factors, a notable difference is only observed in the extent of the strain anisotropy (see Fig. 5).

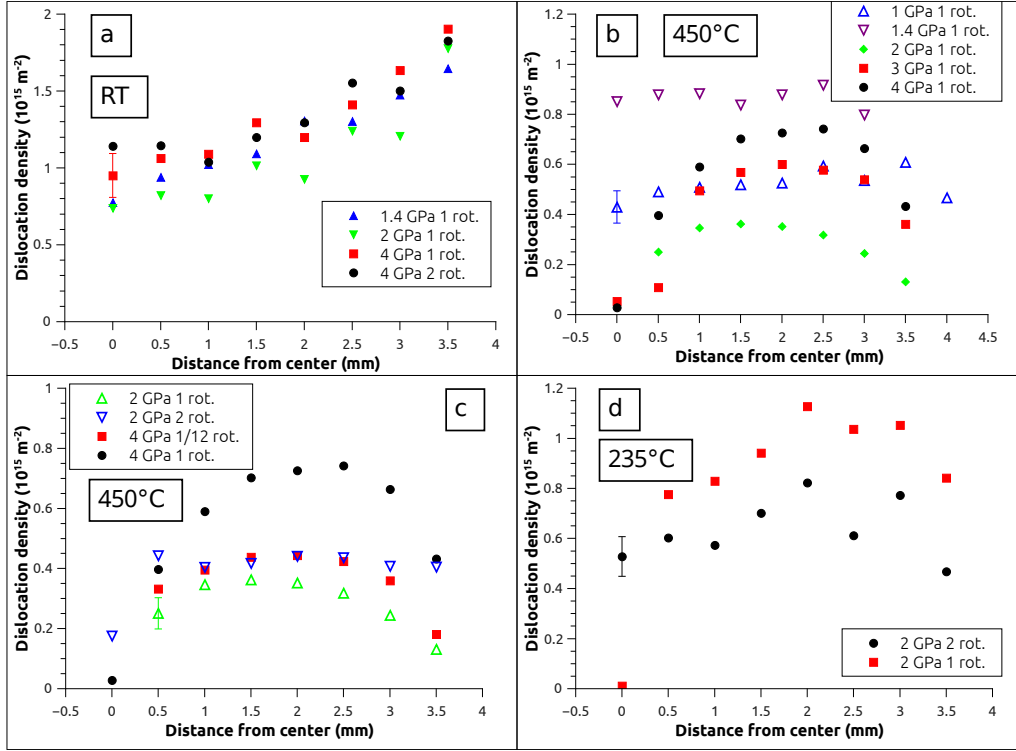


Figure 6: Dislocation densities after HPT-deformation as a function of distance from the rotation axis. (a) samples deformed at room temperature under 1.4, 2 and 4 GPa confining pressure respectively for one rotation and one sample deformed at 4 GPa for two rotations. (b) samples deformed at 450°C for one rotation under 1, 1.4, 2, 3 and 4 GPa confining pressure. (c) samples deformed at 450°C under 2 GPa for 1 and 2 rotations, and under 4 GPa for 1/12 and 1 rotations respectively. (d) samples deformed at 235°C under 2 GPa confining pressure for 1 and 2 rotations.

4.2. Dislocation Density

The dislocation density shows a systematic variation with temperature, pressure and radial distance from the rotation axis, hence, with strain and strain rate (see Fig. 6). For a given strain and strain rate, lower temperatures and higher pressures generally result in higher dislocation densities, whereby the influence of varying pressures is more pronounced at higher temperatures than at lower temperatures. Samples deformed at room temperature show a monotonic increase in dislocation density with increasing radial distance from the rotation axis. In contrast, samples deformed at 235°C and 450°C exhibit a more complex behavior. After an initial increase of the dislocation density with

distance from the rotation axis in samples deformed for up to one rotation the dislocation density saturates and even decreases with increasing distance from the rotation axis. At 235°C the saturation of dislocation density is reached at a higher radial distance than at 450°C.

4.2.1. Deformation at room temperature

The monotonic, almost linear increase of dislocation density with increasing distance from the sample center at room temperature can be seen in Fig. 6a. The samples deformed under 4 GPa for one and two rotations do not show any systematic differences in dislocation density except for strains smaller than about 10 (corresponding to a radial distance of < 1 mm), where the dislocation density is slightly higher after two rotations than after one rotation. The similarity of dislocation densities from one and two rotations at radial distances larger than 1 mm indicates that the shear strain rate rather than strain is the parameter controlling dislocation density. In addition, the dislocation density shows a weak dependence on the confining pressure. The samples deformed under the highest applied pressure of 4 GPa exhibit a higher dislocation density than the samples deformed under 1 and 2 GPa pressure. Interestingly, the sample deformed under 1.4 GPa displays consistently a slightly higher dislocation density than the one deformed under 2 GPa pressure, for most measurement points this effect is within the experimental error, though.

4.2.2. Deformation at 450°C

For samples deformed at elevated temperatures, the confining pressure has a more pronounced influence on the resulting dislocation densities (see Fig. 6b). Two different pressure regimes can be distinguished based on the evolution of dislocation density with applied strain: At 1 and 1.4 GPa confining pressure and one rotation the dislocation density saturates with increasing radial distance from the center after an initial increase along the first mm, where the dislocation density is higher at 1.4 GPa than at 1 GPa (see Fig. 6b empty symbols).

Samples deformed under confining pressures ranging from 2 to 4 GPa for one rotation show a markedly different behavior (see Fig. 6b filled symbols). After an initial increase with distance from the center the dislocation density saturates only at higher strains and even decreases towards the edge of the sample. Similarly to the samples deformed in the low-pressure regime, the dislocation density shows a clear pressure dependence. With

increasing pressure the dislocation density increases for a given radial distance, and the maximum in the dislocation density shifts towards successively higher radial distances from the center.

In both, the low-pressure and the high-pressure regimes, higher confining pressures lead to higher dislocation densities. The trend of increasing dislocation densities with increasing confining pressure is, however, persistent only within each of the two pressure regimes. The pressure effect shows a discontinuity at the boundary between the two regimes between 1.4 and 2 GPa, where a jump from dislocation densities of $9 \pm 1.4 \times 10^{14} \text{ m}^{-2}$ in the high-pressure limit of the low-pressure regime to a maximum of $3.5 \pm 0.5 \times 10^{14} \text{ m}^{-2}$ in the low-pressure limit of the high-pressure regime occurs.

4.2.3. Deformation at 235°C

Due to the small footprint of the beam at the ALS beamline used for measuring the samples that were deformed at 235°C, the data on the dislocation density are rather scattered. Nonetheless, some insight into the evaluation of the dislocation density during deformation at 235°C could be gained. Fig. 6d shows two samples deformed under 2 GPa confining pressure for one and two rotations, respectively. As expected, the dislocation densities obtained from deformation at 235°C are between those of the samples deformed at room temperature and at 450°C. The dislocation density shows an initial increase with radial distance from the rotation axis before it saturates and decreases again. This behavior is similar to what has been observed in the samples deformed at 450°C and pressures of at least 2 GPa. In contrast to the samples deformed at 450°C, in the samples deformed at 235°C the dislocation density is higher and decreases only further away from the rotation axis and not as strongly.

4.3. Coherently scattering domain size

We describe the CSD-size distribution as determined by line profile analysis with a single parameter. To this end, the area averaged mean crystallite size $\langle x \rangle_{area}$ is used. It characterizes the CSD-size by an area weighted mean grain diameter similar to the size parameters extracted from grain size evaluations by microscopy. It can be derived from the m and σ parameters of the fitted size distribution according to (Ungár, 2004):

$$\langle x \rangle_{area} = m \exp(2.5\sigma^2) \quad (9)$$

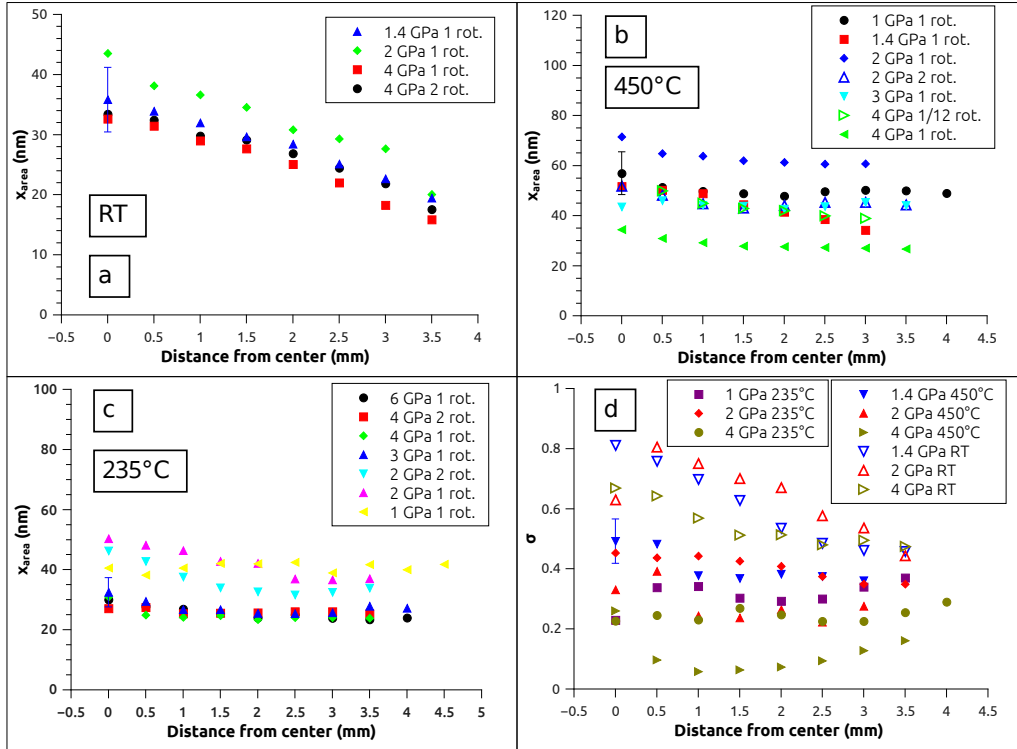


Figure 7: CSD size expressed as area weighted size parameter $\langle x \rangle_{area}$ (a-c) and width of the CSD size distributions (d) after HPT deformation as a function of the distance from the rotation axis. (a) samples deformed at room temperature under 1.4, 2 and 4 GPa confining pressure, respectively, for one rotation and one sample deformed at 4 GPa for two rotations. (b) samples deformed at 450°C for one rotation under 1, 1.4, 2, 3 and 4 GPa confining pressure and under 2 GPa for 2 rotations and under 4 GPa for 1/12 rotation. (c) samples deformed at 235°C under 1, 2, 3, 4 and 6 GPa confining pressure for 1 rotation and 2 and 4 GPa for two rotations. (d) Width of the CSD size distribution σ for samples deformed for one rotation at room temperature and at 450°C applying confining pressures of 1.4, 2 and 4 GPa and at 235°C applying confining pressures of 1, 2 and 4 GPa.

Similarly to the dislocation density, the CSD size shows a strong dependence on both the pressure and temperature conditions prevailing during deformation, where low temperatures and high pressures generally lead to small CSD sizes (see Fig. 7).

4.3.1. Deformation at room temperature

Just as is the case with the dislocation density, the domain size does not show a saturation but decreases linearly with increasing radial distance from the center in samples deformed at room temperature (Fig. 7a). The decrease in $\langle x \rangle_{area}$ is not due to a shift in the median m of the size distribution function, it is rather due to the decreasing width of the distribution, demonstrating that the distribution of the CSD size becomes more narrow with increasing radial distance from the center. This can be seen in Fig. 7d, where the σ parameter, which reflects the width of the distribution for a given value of m , decreases down to a value of about 0.5 in concordance with the CSD size. Yet this value is still high given the small CSD size, exemplifying the heterogeneous character of the CSDs caused by deformation at room temperature. The samples deformed at 4 GPa for one and two rotations respectively display no significant difference, showing that at room temperature the CSD size evolution is controlled by the strain rate rather than by strain. Both the CSD size and the distribution width show the same weak influence of the confining pressure as the dislocation density, where higher pressures generally lead to smaller CSD sizes and narrower distributions. Just as in the case of the dislocation density, the pressure dependence exhibits an anomaly between 1.4 and 2 GPa, where the CSD size and width are slightly smaller (within the measurement error) at 1.4 than at 2 GPa.

4.3.2. Deformation at 450°C

The evolution of the CSD size distribution during deformation at elevated temperatures differs markedly from the room temperature case. Fig. 7b shows the CSD sizes of samples deformed at 1, 1.4, 2, 3 and 4 GPa at 450°C for one rotation. The CSD size decreases with increasing pressure in the range from 2 to 4 GPa confining pressure similar to the samples deformed at room temperature, but at 450°C the pressure dependence is more pronounced. The CSD size of the samples deformed at 1 and 1.4 GPa confining pressure lies in between the values for the samples deformed under 2 and 4 GPa. With the exception of the sample deformed at 1.4 GPa, the CSD size saturates after an initial distinct decrease with distance from the center.

To investigate the strain and strain rate dependence of the CSD-size evolution, one sample was deformed under 4 GPa confining pressure to 1/12 of a rotation, whereas another sample was deformed under 2 GPa confining pressure to 2 rotations. It is seen in Figure 7b that neither data points with equal strain rate but different strain nor data points with equal strain but different strain rates exhibit the same CSD size. This indicates that, in contrast to the room temperature case, neither strain nor strain rate alone are the controlling parameters.

The width of the CSD size distribution is smaller than for the room temperature case despite of larger CSD sizes, and it displays a marked pressure dependence. It shows the same strain dependence as the $\langle x \rangle_{area}$ parameter, remaining constant after an initial decrease. The size distribution broadens with decreasing pressure, with the sample deformed under 1 GPa pressure exhibiting the broadest distribution (see Fig. 7d).

4.3.3. Deformation at 235°C

As expected, the values for the CSD size parameter of samples deformed at 235°C lie between those of the samples deformed at room temperature and those deformed at 450°C. Fig. 7c shows the CSD size for samples deformed under 1 to 6 GPa confining pressure for one rotation as well as for samples deformed under 2 and 4 GPa confining pressure for two rotations. Similar to the situation at 450°C the CSD size saturates after an initial decrease with radial distance from the center. In contrast to the samples deformed at 450°C, the effect of pressure variations is more muted and becomes insignificant beyond 3 GPa, where the CSD is 25-30 nm at radial distances beyond 1 mm. The samples deformed at 2 GPa exhibit a significantly larger CSD size, which is still smaller than the corresponding values of the samples deformed at 450°C by almost a factor of 2. In addition, the initial decrease of the CSD size with increasing distance from the center is much more pronounced than at higher pressures. The sample deformed under 1 GPa pressure displays a different behavior, just as it is the case for the other deformation temperatures. Its CSD size does not show any dependence on the measurement position, and close to the center it is smaller than the CSD size of the samples deformed at 2 GPa pressure.

To differentiate between the effect of strain and strain rate two samples were deformed under 2 and 4 GPa pressure for two rotations. As Fig. 7c shows, the two samples deformed under 4 GPa demonstrate no significant difference regarding their CSD size indicating that after the initial deformation stage the CSD size is independent of strain and strain

rate similar to the room temperature case. In contrast, the CSD size of the sample deformed under 2 GPa for two rotations is notably smaller than the CSD size of the sample deformed for one rotation. This conforms with the samples deformed at 450°C, where neither strain nor strain rate are the sole defining parameters for the CSD size.

The width of the CSD size distribution of these samples is well below the room temperature case and similar to the width of the CSD size distribution of the samples deformed at 450°C. Fig. 7d shows that the size distribution becomes more homogeneous with increasing pressure albeit not as pronouncedly as in the 450°C case. The width of the CSD size distribution shows a weak dependence on the radius, this dependence further decreases with increasing pressure.

5. Discussion

5.1. Slip system analysis

The identification of $r\{10\bar{1}4\}\langle\bar{2}021\rangle$ as the dominant active slip system agrees well with earlier studies on experimentally deformed calcite (De Bresser and Spiers, 1997; Turner et al., 1954; Barber et al., 2010). In these studies slip on $r\{10\bar{1}4\}\langle\bar{2}021\rangle$ was found to be one of the most important mechanisms of plastic deformation in calcite at temperatures up to 800 K. According to De Bresser and Spiers (1997) this slip system has the lowest critically resolved shear stress (CRSS) among the known slip systems in calcite for the deformation temperatures and strain rates relevant to this study.

The anisotropy of the experimentally determined dislocation contrast factors reflects the anisotropy of the theoretically calculated contrast factors very well in a qualitative sense. The magnitude of the strain anisotropy is, however, significantly lower for the experimentally determined than for the theoretically calculated contrast factors (see Fig. 5). It is known from TEM investigations on calcite that in bright field images the dislocation contrast used for the Burgers vector analysis does not vanish, as it is the case in metals, when the Burgers and diffraction vectors are perpendicular (Barber et al., 2007). One of the reasons for the difference between the dislocation contrast derived from the model and the experimental values lies in the non-negligible proportion of covalent bonding in calcite. While the bonds between the calcium ions and the carbonate groups are primarily of ionic character, the bonds between the carbon and oxygen within the carbonate groups are of more covalent nature. Therefore a non-negligible fraction of the electron density in the carbonate groups lies between the C- and O-ions. This is in

conflict with the model assumption of a spherically symmetric electron density around the ions underlying the kinematical theory of diffraction used in XPA (Ungár, 1999).

Moreover, due to the reduced mobility of point defects during plastic deformation under high confining pressure, the concentration of vacancies during HPT deformation is much higher than the equilibrium concentration at the same pressure and temperature conditions (Zehetbauer et al., 2003, 2006). High concentrations of point defects in the vicinity of dislocation cores naturally leads to a relaxation of the strain fields and dampening of the strain broadening of the Bragg peaks (Bullough and Newman, 1970), which diminishes the anisotropy of the dislocation contrast determined in diffraction experiments (Barber et al., 2007).

It is important to note, that several experiments were performed at $P-T$ conditions, where the metastable high-pressure polymorphs of CaCO_3 were present during deformation, yet no change in dislocation contrast was observed when crossing from the stability field of calcite into the stability fields of the high-pressure polymorphs. Our results suggest that in the high-pressure polymorphs dislocation glide operates in a similar manner as in calcite. In particular, our results indicate that in the high pressure polymorphs the glide planes and directions correspond to the $r\{10\bar{1}4\}$ lattice plane and the $\langle\bar{2}021\rangle$ direction in calcite.

Twinning on $e\{10\bar{1}8\}$ planes is an important deformation mechanism in calcite. In particular, at room temperature the CRSS for $e\{10\bar{1}8\}$ twinning is substantially lower than for dislocation glide on $r\{10\bar{1}4\}\langle\bar{2}021\rangle$. Twinning on $e\{10\bar{1}8\}$ planes certainly contributed to deformation during the HPT experiments. The maximum shear strain that can be accommodated by e -twinning in calcite is 0.69 (Schmid et al., 1987). In comparison, the local shear strain attained during HPT of one rotation for a radial distance of 1 mm from the rotation axis is about 10. Therefore, in our experiments the contribution of twinning to the bulk deformation is minute. In addition, due to the low density of twin boundaries the contribution of twinning to Bragg peak broadening is negligible. Therefore, in our case information on twinning cannot be extracted from XPA, and no quantitative relationship between the contribution from twinning and from dislocation glide can be given.

5.2. Influence of temperature on microstructure evolution

It emerges from our experiments that the temperature has a strong influence on microstructure evolution during deformation (see Figs. 6, 7, and 8). Not only are the

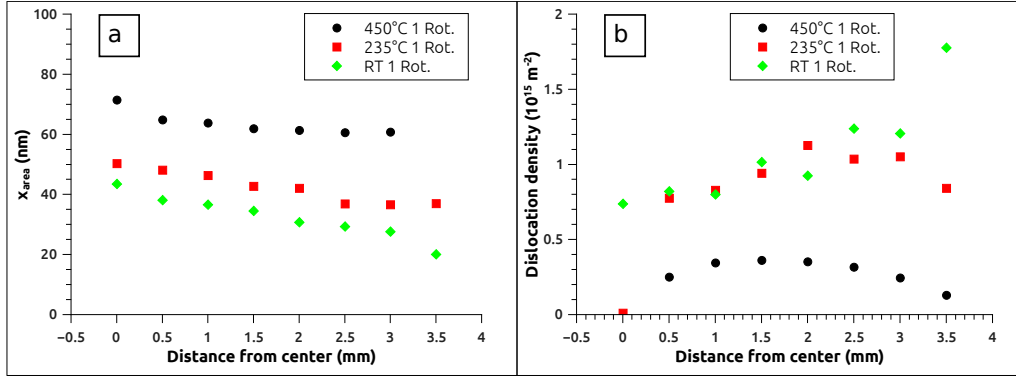


Figure 8: Temperature influence on (a) CSD size and (b) dislocation density in samples deformed under 2 GPa confining pressure for one rotation.

dislocation densities higher and the CSD sizes smaller after deformation at room temperature than after deformation at elevated temperatures, but there are also systematic differences in the evolution of these parameters as a function of the applied strain. In samples deformed for one rotation at room temperature the dislocation density shows a monotonic increase with increasing strain, that is with radial distance from the rotation axis, and does not exhibit a saturation with increasing strain even at shear strains of 40 or higher (Fig. 8b). In contrast, if samples are deformed for one rotation at elevated temperatures, the dislocation density saturates at a certain strain and beyond saturation even decreases with increasing strain. Similarly, at room temperature the CSD size steadily decreases with increasing strain in samples deformed for one rotation, whereas at elevated temperatures it saturates after an initial decrease with increasing strain (see Figs. 7 and 8a). The experimentally observed microstructure evolution reflects successive accumulation of defects and diminution of the CSD size during deformation at low temperature and considerably more efficient recovery and eventually attainment of a dynamic equilibrium between nucleation and annihilation of dislocations during deformation at elevated temperatures.

Microstructure evolution during deformation is determined by the competition between deformation-induced nucleation of dislocations and recovery through their organization into energetically favorable arrangements such as (sub)grain boundaries and eventually annihilation, both of which require dislocation glide and climb (Passchier and Trouw, 1996). The strong influence of temperature can be explained by the temperature-

dependence of the mobility of dislocations. Dislocation climb is a non-conservative motion of a dislocation in the sense that it requires supply or removal of point defects at the dislocation core by diffusion and is thus a thermally activated process. Although during deformation by HPT the concentration of point defects is substantially higher than in thermodynamic equilibrium (Zehetbauer et al., 2006), their mobility is very limited at low temperature. This renders dislocation climb extremely sluggish, and formation of energetically favorable dislocation structures via polygonalization and the annihilation of dislocations are very limited. In contrast, these processes are very efficient at elevated temperatures. In addition, even though dislocation glide is a conservative mode of dislocation motion and does not involve long-range diffusion of point defects, it still shows considerable temperature dependence (De Bresser and Spiers, 1997).

The CSDs that are observed after deformation at 450°C may be interpreted as the characteristic sizes of dislocation cells, consisting of strain-free domains separated by thin regions of high dislocation density, which are produced during recovery of deformed materials (Mughrabi, 1983). The CSD size obtained by XPA in HPT-deformed metals and alloys very likely corresponds to the size of these dislocation cells (Ungár, 2005). TEM studies on deformed calcite have revealed the formation of dislocation cell structures similar to those found in metals (Barber and Wenk, 1979; Barber et al., 2010; Rybacki et al., 2013). The heterogeneous arrangement of dislocations in these dislocation cells leads to a reduction of lattice strain caused by dislocations, due to the screening of the strain fields of dislocations by neighbouring dislocations with opposite orientation. Higher deformation temperatures promotes the formation of these cell structures in calcite in a twofold manner. On the one hand, the CRSS of slip systems in calcite is strongly temperature dependent, especially so at low temperatures (De Bresser and Spiers, 1997). In order to build dislocation cell structures multiple slip systems need to be active. This may necessitate, depending on the grain orientation, secondary slip on a slip system other than one of the three $r\{10\bar{1}4\}\langle\bar{2}021\rangle$ slip systems, which is enhanced at high temperatures. On the other hand, arrangement of dislocations into the energetically favorable cell arrangements requires dislocation climb, which is thermally activated. A lack of active thermally activated crystal-plastic deformation mechanisms at low temperatures is reflected by the relatively small CSD sizes and their rather wide distribution after deformation at room temperature as compared to larger and more homogeneously distributed CSD sizes in the samples deformed at 450°C (see Fig. 7). The saturation of the CSD size with increasing

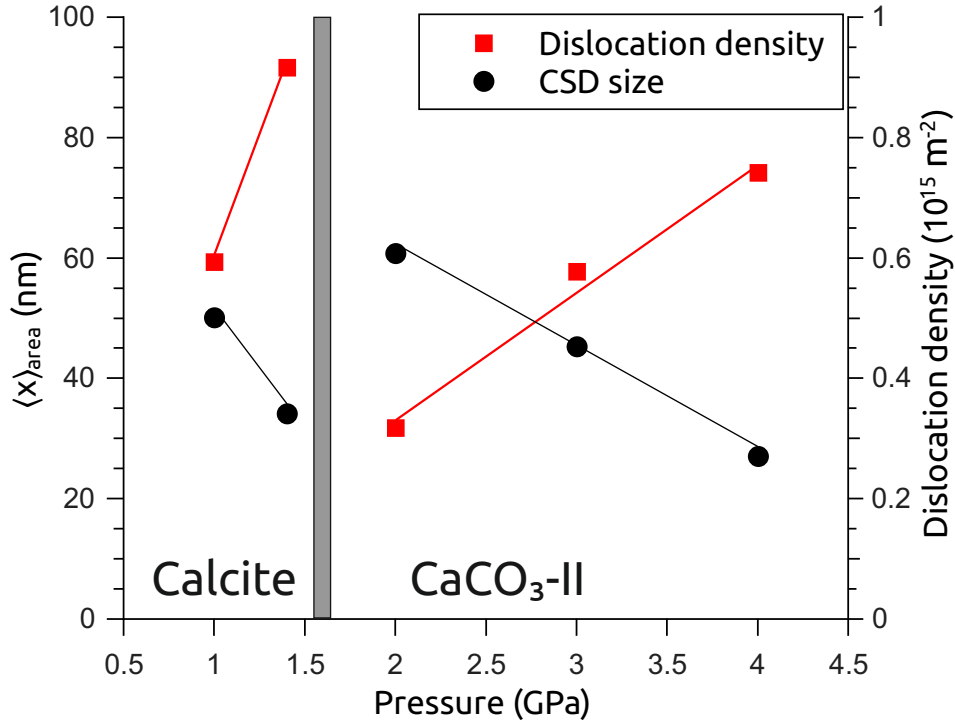


Figure 9: Pressure influence on CSD size and dislocation density in samples deformed at 450°C for one rotation. The measurements were taken 3 mm from the center corresponding to a shear strain of 31 and a shear strain rate of $1 \times 10^{-2} \text{ s}^{-1}$.

strain after deformation at 235°C and 450°C is similar though less pronounced to the strain-dependence of crystallite sizes in HPT deformed copper (Hebesberger et al., 2005).

The high dislocation densities observed after deformation at room temperature do not necessarily imply that dislocation glide is the prominent deformation mechanism. Calcite twinning is favored compared to dislocation glide at low temperatures, since the CRSS for twinning is much lower than for dislocation glide. TEM and etching studies have shown that mechanical twinning in calcite is accompanied by high dislocation densities around the twin boundaries and within the twins (Keith and Gilman, 1960; Barber and Wenk, 1979). The high dislocation density may therefore result from sessile dislocations that are at least in part due to twinning.

5.3. Effect of hydrostatic pressure on deformation

Our experiments that have been performed over a pressure range from 1 to 6 GPa reveal that apart from the temperature also the confining pressure applied during HPT has a significant influence on the evolution of the microstructural parameters. Four different polymorphs of CaCO_3 are expected to have been present during deformation at the different temperatures and confining pressures applied (see Table 1). According to Pippinger et al. (2015) calcite is stable at low pressures, and at about 1.2 to 1.6 GPa, depending on the temperature, it transforms to $\text{CaCO}_3\text{-II}$, and at pressures in excess of about 2.2 GPa $\text{CaCO}_3\text{-III}$ and $\text{CaCO}_3\text{-IIIb}$ become the stable polymorphs, where $\text{CaCO}_3\text{-III}$ and $\text{CaCO}_3\text{-IIIb}$ are confined to temperatures below about 250°C. The boundary between the stability fields of calcite and $\text{CaCO}_3\text{-II}$ has been studied for temperatures up to 700°C by Kondo et al. (1972), who place it at 1.5 GPa for 250°C and at 1.6 GPa for 450°C. For both, the experiments done in the low-pressure regime in the stability field of calcite and for the experiments done in the high-pressure regime, within the stability fields of $\text{CaCO}_3\text{-II}$, $\text{CaCO}_3\text{-III}$ and $\text{CaCO}_3\text{-IIIb}$ an increase in the confining pressure leads to an increase of the dislocation densities and a decrease of the CSD sizes, where the effect is more pronounced at high temperatures than at low temperatures. This pressure effect is due to the influence of pressure on the crystal lattice and the elastic anisotropy (Poirier, 1985). The formation of dislocations and point defects leads to excess volume, and work must be done against the applied pressure during the creation and movement of such defects (Zehetbauer et al., 2003). Elevated hydrostatic pressure therefore influences the mobility of dislocations in a similar way as reduced temperature. The pressure effect is generally less significant for glide-controlled creep than for thermally activated recovery processes (Poirier, 1985). A qualitative indication of the similarity between the effects of reduced temperature and elevated pressure is given by the shift of the maximum dislocation density towards higher radial distances, which is similarly produced by either a pressure increase from 2 to 3 or 4 GPa at 450°C or a temperature decrease from 450°C to 235°C at 2 GPa (see Fig. 6b,d).

The trend of increasing dislocation density and decreasing CSD size with increasing pressure is broken at the supposed pressure of the calcite to $\text{CaCO}_3\text{-II}$ transformation. In our experiments, the dislocation density shows a sharp drop and the CSD size shows a sharp increase with a change in pressure from 1.4 to 2 GPa at room temperature and at 450°C (see Fig. 9) and with a change in pressure from 1 to 2 GPa at 235°C. The anomaly

in the pressure effect is more pronounced at high temperatures than at low temperatures. At room temperature the CSD size at 1.4 GPa is consistently smaller by about 10-20 % than at 2 GPa for similar local strain, which is close to the measurement error of 15 %. The relative difference in the dislocation density is even smaller. At 450°C the CSD sizes at 1 and 1.4 GPa are 20-30 % and 30-80 %, respectively, smaller than at 2 GPa. The effect on the dislocation density at 450°C is even more pronounced with the dislocation densities being 40 % and 150 % higher at 1 and 1.4 GPa, respectively, than at 2 GPa.

In addition to the quantitative change, the evolution of the dislocation density with strain is also qualitatively different for deformation in the low- and high-pressure regimes (see Fig. 6). In the low-pressure regime of 1 and 1.4 GPa the dislocation density develops in accordance with the results from earlier studies on deformation in the stability field of calcite. For example, based on torsion experiments on Carrara marble at 1000 K and at 300 MPa confining pressure Pieri et al. (2001a,b) found that a steady state flow stress, a stable texture and an equilibrium grain size are reached at shear strains between 2 and 5. This agrees well with the dislocation density evolution in our samples, where the saturation is reached at a shear strain of about 5. In the high-pressure regime at pressures of 2 GPa and higher the dislocation density does not reach a saturation for samples deformed for one rotation even though the shear strain on the sample rim exceeds 40. Comparison of the samples deformed under 2 GPa for one and two rotations, respectively, reveals that after two rotations the dislocation density attains saturation, where the dislocation density at saturation is slightly higher than the maximum value for one rotation (see Fig. 6c). Furthermore, in the sample deformed under 4 GPa to 30° (1/12 rotation) the dislocation density shows similar qualitative behavior as in the sample deformed at 4 GPa for one rotation, with the only difference that for a given strain rate the dislocation density is lower in the sample deformed for 1/12 rotation than in the sample deformed for one rotation (see Fig. 6c). This peculiar behavior cannot be explained solely based on XPA. Referring to preliminary results from crystal orientation imaging with electron backscatter diffraction (EBSD) it may, however, be hypothesized that at high strain-rates, that is at large radial distance from the rotation axis, the deformation is preferentially accommodated by dynamic recrystallization and the associated formation of high-angle grain boundaries. Immediately after their formation the grains that are newly generated during this process have lower dislocation densities than the relict porphyroclasts. The porphyroclasts are more likely preserved at low strain and

strain rate, that is at lower radial distances from the rotation axis. The variation of the dislocation densities observed with increasing radial distance is thus likely due to the combined effects of two processes. The initial increase in the dislocation density with radial distance reflects the successive loading with dislocations during progressive crystal plastic deformation of the pre-existing grains. This trend of increasing dislocation density is then truncated by the successive formation of new grains by dynamic recrystallization at high strains and strain rates occurring at higher radial distances from the rotation axis. This effect is likely to be obliterated through the progressive transformation of the porphyroclasts into recrystallized grains and the successive generation of dislocations within the recrystallized grains during ongoing deformation, as is indicated by the rather homogenous distribution of dislocation densities after deformation for two rotations (see Fig. 6c).

5.4. *Implications for natural deformation*

When deformation proceeds by dislocation creep, the relationship between dislocation density and applied stress can be used to infer the applied stress from deformation microstructures. Microphysical models for dislocation creep predict that the flow stress is proportional to the square root of the dislocation density (Kohlstedt and Weathers, 1980). This naturally implies that once steady state flow is reached, the dislocation density stays constant and vice versa (Kohlstedt and Weathers, 1980; De Bresser, 1996). Our results indicate that at 450°C in the CaCO₃-II stability field steady state deformation and thus constant microstructural parameters are only attained at significantly higher strain than at 450°C in the calcite stability field and that the microstructural parameters associated with steady state deformation are strain rate sensitive at least at strain rates between 10⁻² and 10⁻³ s⁻¹. In addition, the jump in the dislocation density between 1.4 and 2 GPa suggests a weakening of carbonate rocks, when the boundary between the calcite and CaCO₃-II stability fields is crossed in the absence of aragonite formation.

Although the temperatures in the earth's crust pertaining to the lithostatic pressures, at which the high-pressure polymorphs of CaCO₃ form, usually exceed the deformation temperatures used in this study, the pertinent $P - T$ conditions may nonetheless be reached in nature under specific circumstances. In the case of subduction of old lithosphere into the mantle, extremely low geothermal gradients have been observed. Peacock and Wang (1999) calculated that the temperature of the Pacific plate subducted beneath north-east Japan reaches 200°C only at 50 km depth. Even at more common, higher

geothermal gradients of 10 K/km the $P - T$ conditions of our experiments may locally be generated by tectonic overpressure. Field observations of high-pressure minerals in rocks typical for low-pressure metamorphism (Warren, 2013) and numerical modeling (Mancktelow, 2008; Vrijmoed et al., 2009; Li et al., 2010) have shown that significant overpressures of up to 40 % of the lithostatic pressure may occur for pressures up to 2 GPa. In addition, unusually high pressures may also be generated locally during deformation events on the earth's surface as was inferred from the presence of nanocrystalline $\text{CaCO}_3\text{-II}$ and $\text{CaCO}_3\text{-III}$ in rocks deformed during landslide events (Schaebitz et al., 2015).

Moreover, we could demonstrate that high confining pressure in the GPa range can have a significant influence on the deformation behavior and resulting microstructure also aside from the impact of phase transitions. Earlier studies on deformation at lower confining pressures showed only a minute influence of confining pressure on the flow stress (De Bresser, 2002). It was found by De Bresser (2002) that the flow stress increases by about 1.6 % per 100 MPa in uniaxial compression tests at 800-1000°C and confining pressures between 100 to 600 MPa. In contrast, the influence of varying confining pressures on the inferred flow stress appears to be substantially more pronounced for deformation at about 1 GPa. Applying the aforementioned square root relationship between dislocation density and flow stress to our experiments at 450°C, an increase of the steady state flow stress of about 30 % is inferred for a pressure increase from 1 to 1.4 GPa, which corresponds to an increase of the flow stress of 7.5 % per 100 MPa. At pressures in excess of about 2 GPa the influence of the confining pressure on the inferred flow stress decreases with increasing pressure. This is evident from the fact that in the samples deformed at 450°C for one rotation the flow stress inferred for the maximum dislocation density increases only by about 30 % with a pressure increase from 2 to 3 GPa (3 % per 100 MPa) and by about 10 % with a pressure increase from 3 to 4 GPa (1 % per 100 MPa).

6. Conclusions

Calcite powder was pressed and deformed to high strain at confining pressures of 1 to 6 GPa and temperatures ranging from room temperature to 450°C using high-pressure torsion. The resulting microstructures were characterized by synchrotron based X-ray diffraction experiments and analyzed by X-ray line profile analysis.

The analysis of the strain anisotropy as obtained from Bragg peak broadening showed that $r\{10\bar{1}4\}(\bar{2}021)$ with edge character is the dominant slip system for deformation under the pressure, temperature and strain rate conditions applied in this study. The dislocation contrast does not show any change, when the $P-T$ conditions of deformation are shifted from the stability field of calcite to the stability fields of the high pressure polymorphs $\text{CaCO}_3\text{-II}$, $\text{CaCO}_3\text{-IIIb}$ and $\text{CaCO}_3\text{-III}$, indicating that slip in these phases operates in a similar manner as in calcite.

In addition, the influence of pressure and temperature on the evolution of the microstructure during HPT could be established. Higher temperature allows for the development of a homogeneous and stable CSD size whereas at room temperature recovery and dynamic recrystallization are greatly hindered leading to much broader CSD size distributions. With respect to the effect of pressure a low-pressure regime defined by the stability field of calcite and a high-pressure regime coinciding with the stability fields of the high pressure CaCO_3 polymorphs is discerned. Within the stability field of either calcite or of the high-pressure CaCO_3 polymorphs increasing pressure leads to higher dislocation densities and smaller CSD sizes, where the effect diminishes with lower temperature and higher pressure. This trend is, however, broken at the calcite to $\text{CaCO}_3\text{-II}$ transformation, where an increase in pressure leads to a sudden increase in CSD size and a concomitant drop in the dislocation density. This effect is more pronounced at elevated temperatures than at room temperature.

Furthermore, at pressures below the calcite to $\text{CaCO}_3\text{-II}$ transition the dislocation density saturates after an applied shear strain of about 10 in agreement with earlier studies on deformation at lower pressures. At pressures above the calcite to $\text{CaCO}_3\text{-II}$ transition the strain and strain-rate dependence of microstructural parameters is more complex and governed by the effects of several competing processes including the successive accumulation of lattice strain within coherently scattering domains and potentially the formation of high-angle grain boundaries through dynamic recrystallization.

The effect of varying confining pressures is secondary to changes in temperature, but can still be relevant even within the stability field of a single phase. It is most significant at high temperatures and at pressures of about 1 GPa, and it diminishes with decreasing temperatures and with decreasing and increasing pressures. The drop of the dislocation densities with increasing pressure at the calcite to $\text{CaCO}_3\text{-II}$ transition implies a weakening of carbonate-bearing rocks at these conditions.

7. Acknowledgements

The authors acknowledge funding by the University of Vienna doctoral school Deformation of Geological Materials (DOGMA) (IK052) and the project of the Austrian Science fund (FWF): I474-N19, as part of the international DFG-FWF funded research network FOR741-DACH. This research used beamline 12.3.2 at the Advanced Light Source, which is a DOE Office of Science User Facility under contract no. DE-AC02-05CH11231. Andrij Grytsiv of the University of Vienna is thanked for provision of access to the powder press at the Faculty of Chemistry, University of Vienna. Tamas Ungár is thanked for helpful discussions on the topic of XPA.

8. References

- Antao, S., Hassan, I., Mulder, W., Lee, P., Toby, B., 2009. The $R\bar{3}c \rightarrow R\bar{3}m$ transition in nitratine, NaNO_3 , and implications for calcite, CaCO_3 . *Physics and Chemistry of Minerals* 36 (3), 159–169.
- Barber, D. J., Wenk, H.-R., 1979. Deformation twinning in calcite, dolomite, and other rhombohedral carbonates. *Physics and Chemistry of Minerals* 5 (2), 141–165.
- Barber, D. J., Wenk, H.-R., Gomez-Barreiro, J., Rybacki, E., Dresen, G., Feb. 2007. Basal slip and texture development in calcite: new results from torsion experiments. *Physics and Chemistry of Minerals* 34 (2), 73–84.
- Barber, D. J., Wenk, H.-R., Hirth, G., Kohlstedt, D. L., 2010. Dislocations in Minerals. In: *Dislocations in Solids*. Vol. 16. Elsevier, Ch. 95, pp. 171–232.
- Barnhoorn, A., Bystricky, M., Burlini, L., Kunze, K., 2004. The role of recrystallisation on the deformation behaviour of calcite rocks: Large strain torsion experiments on Carrara marble. *Journal of Structural Geology* 26 (5), 885–903.
- Barnhoorn, A., Bystricky, M., Burlini, L., Kunze, K., 2005. Post-deformational annealing of calcite rocks. *Tectonophysics* 403 (1-4), 167–191.
- Bestmann, M., Prior, D. J., Oct. 2003. Intragranular dynamic recrystallization in naturally deformed calcite marble: diffusion accommodated grain boundary sliding as a result of subgrain rotation recrystallization. *Journal of Structural Geology* 25 (10), 1597–1613.
- Bridgman, P. W., 1936. Shearing Phenomena at High Pressure of Possible Importance for Geology. *The Journal of Geology* 44 (6), 653–669.
- Bridgman, P. W., 1938. The high pressure behavior of miscellaneous minerals. *American Journal of Science* 237 (1), 7–18.
- Bullough, R., Newman, R., 1970. The kinetics of migration of point defects to dislocations. *Reports on progress in physics* 33 (1), 101.
- Burkhard, M., 1993. Calcite twins, their geometry, appearance and significance as stress-strain markers and indicators of tectonic regime: a review. *Journal of Structural Geology* 15 (3-5), 351–368.
- Casey, M., Kunze, K., Olgaard, D., FEB-MAR 1998. Texture of Solnhofen limestone deformed to high strains in torsion. *Journal of Structural Geology* 20 (2-3), 255–267.

- Dandekar, D. P., Aug. 1968. Pressure Dependence of the Elastic Constants of Calcite. *Physical Review* 172 (3), 873–877.
- De Bresser, J., 1996. Steady state dislocation densities in experimentally deformed calcite materials: Single crystals versus polycrystals. *Journal of Geophysical Research: Solid Earth* 101 (B10), 22189–22201.
- De Bresser, J., Evans, B., Renner, J., 2002. On estimating the strength of calcite rocks under natural conditions. *Geological Society Special Publication* 200, 309–329.
- De Bresser, J. H. P., Dec. 2002. On the mechanism of dislocation creep of calcite at high temperature: Inferences from experimentally measured pressure sensitivity and strain rate sensitivity of flow stress. *Journal of Geophysical Research: Solid Earth* 107 (B12), ECV 4–1–ECV 4–16.
- De Bresser, J. H. P., Spiers, C. J., Apr. 1997. Strength characteristics of the r, f, and c slip systems in calcite. *Tectonophysics* 272, 1–23.
- Dragomir, I., Ungár, T., 2002. Contrast factors of dislocations in the hexagonal crystal system. *Journal of Applied Crystallography* 35 (5), 556–564.
- Fernández, F., Brown, D., Alvarez-Marron, J., Prior, D., PÉrez-EstaÚn, A., 2004. Microstructure and lattice preferred orientation of calcite mylonites at the base of the southern Urals accretionary prism. *Journal of the Geological Society* 161 (1), 67–79.
- Figueiredo, R. B., Pereira, P. H. R., Aguilar, M. T. P., Cetlin, P. R., Langdon, T. G., 2012. Using finite element modeling to examine the temperature distribution in quasi-constrained high-pressure torsion. *Acta Materialia* 60 (6), 3190–3198.
- Fiquet, G., Guyot, F., Itié, J.-P., 1994. High-pressure X-ray diffraction study of carbonates: MgCO_3 , $\text{CaMg}(\text{CO}_3)_2$, and CaCO_3 . *American Mineralogist* 79 (1-2), 15–23.
- Gerya, T., Perchuk, L., Burg, J.-P., 2008. Transient hot channels: perpetrating and regurgitating ultrahigh-pressure, high-temperature crust–mantle associations in collision belts. *Lithos* 103 (1), 236–256.
- Griggs, D. T., Turner, F., Heard, H., 1960. Deformation of Rocks at 500° to 800°C. *Geological Society of America Memoirs* 79, 39–104.
- Hammersley, A. P., 1997. FIT2D: An introduction and overview. ESRF Internal Report ESRF97HA02T.
- Hammersley, A. P., Svensson, S. O., Hanfland, M., Fitch, A. N., Hausermann, D., May 1996. Two-dimensional detector software: From real detector to idealised image or two-theta scan. *High Pressure Research* 14, 235–248.
- Handin, J., Higgs, D. V., Brien, J. K. O., Mar. 1960. Chapter 9: Torsion of Yule Marble Under Confining Pressure. *Geological Society of America Memoirs* 79, 245–274.
- Hebesberger, T., Stüwe, H., Vorhauer, A., Wetscher, F., Pippan, R., Jan. 2005. Structure of Cu deformed by high pressure torsion. *Acta Materialia* 53 (2), 393–402.
- Herwegh, M., de Bresser, J., ter Heege, J., 2005. Combining natural microstructures with composite flow laws: an improved approach for the extrapolation of lab data to nature. *Journal of Structural Geology* 27 (3), 503 – 521.
- Keith, R. E., Gilman, J. J., Jan. 1960. Dislocation etch pits and plastic deformation in calcite. *Acta Metallurgica* 8 (1), 1–10.
- Kerber, M., Schafler, E., Wiczorek, A., Ribarik, G., Bernstorff, S., Ungar, T., Zehetbauer, M., 2009. Synchrotron X-ray line-profile analysis experiments for the in-situ microstructural characterisation

- of SPD nanometals during tensile deformation. *International Journal of Materials Research* 100 (6), 770–774.
- Kohlstedt, D., Weathers, M. S., 1980. Deformation-induced microstructures, paleopiezometers, and differential stresses in deeply eroded fault zones. *Journal of Geophysical Research: Solid Earth* 85 (B11), 6269–6285.
- Kondo, S., Suito, K., Matsushima, S., 1972. Ultrasonic observation of calcite I-II inversion to 700°C. *Journal of Physics of the Earth* 20 (3), 245–250.
- Krivoglaz, M. A., 1969. *Theory of X-Ray and Thermal Neutron Scattering by Real Crystals*. Springer.
- Lee, D. J., Yoon, E. Y., Ahn, D.-H., Park, B. H., Park, H. W., Park, L. J., Estrin, Y., Kim, H. S., 2014. Dislocation density-based finite element analysis of large strain deformation behavior of copper under high-pressure torsion. *Acta Materialia* 76, 281–293.
- Li, Z., Gerya, T., BURG, J.-P., 2010. Influence of tectonic overpressure on P–T paths of HP–UHP rocks in continental collision zones: thermomechanical modelling. *Journal of Metamorphic Geology* 28 (3), 227–247.
- Mancktelow, N. S., 2008. Tectonic pressure: theoretical concepts and modelled examples. *Lithos* 103 (1), 149–177.
- Martinez-Garcia, J., Leoni, M., Scardi, P., Mar. 2009. A general approach for determining the diffraction contrast factor of straight-line dislocations. *Acta Crystallographica Section A Foundations of Crystallography* 65 (2), 109–119.
- Merlini, M., Hanfland, M., Crichton, W., Jun. 2012. CaCO₃-III and CaCO₃-VI, high-pressure polymorphs of calcite: Possible host structures for carbon in the Earth’s mantle. *Earth and Planetary Science Letters* 333-334, 265–271.
- Merrill, L., Bassett, W. A., 1975. The crystal structure of CaCO₃(II), a high-pressure metastable phase of calcium carbonate. *Acta Crystallographica Section B: Structural Crystallography and Crystal Chemistry* 31 (2), 343–349.
- Mughrabi, H., 1983. Dislocation wall and cell structures and long-range internal stresses in deformed metal crystals. *Acta metallurgica* 31 (9), 1367–1379.
- Passchier, C. W., Trouw, R. A., 1996. *Microtectonics*. Vol. 2. Springer.
- Paterson, M., Olgaard, D., Sep 2000. Rock deformation tests to large shear strains in torsion. *Journal of Structural Geology* 22 (9), 1341–1358.
- Peacock, S. M., Wang, K., 1999. Seismic Consequences of Warm Versus Cool Subduction Metamorphism: Examples from Southwest and Northeast Japan. *Science* 286 (5441), 937–939.
- Pieri, M., Burlini, L., Kunze, K., Stretton, I., Olgaard, D., Sep 2001a. Rheological and microstructural evolution of Carrara marble with high shear strain: results from high temperature torsion experiments. *Journal of Structural Geology* 23 (9), 1393–1413.
- Pieri, M., Kunze, K., Burlini, L., Stretton, I., Olgaard, D., Burg, J., Wenk, H., Jan 2001b. Texture development of calcite by deformation and dynamic recrystallization at 1000 K during torsion experiments of marble to large strains. *Tectonophysics* 330 (1-2), 119–140.
- Pippinger, T., Miletich, R., Merlini, M., Lotti, P., Schouwink, P., Yagi, T., Crichton, W., Hanfland, M., 2015. Puzzling calcite-III dimorphism: Crystallography, high-pressure behavior, and pathway of single-crystal transitions. *Physics and Chemistry of Minerals* 42 (1), 29–43.
- Poirier, J.-P., 1985. Creep of crystals: high-temperature deformation processes in metals, ceramics and

- minerals. Cambridge University Press.
- Renner, J., Evans, B., Siddiqi, G., Dec. 2002. Dislocation creep of calcite. *Journal of Geophysical Research: Solid Earth* 107 (B12), ECV 6–1–ECV 6–16.
- Ribárik, G., 2008. Modeling of diffraction patterns based on microstructural properties. Ph.D. thesis, Eötvös Loránd University.
- Ribárik, G., Gubicza, J., Ungár, T., 2004. Correlation between strength and microstructure of ball-milled Al-Mg alloys determined by X-ray diffraction. *Materials Science and Engineering A* 387-389 (1-2 SPEC. ISS.), 343–347.
- Ribárik, G., Ungár, T., Gubicza, J., 2001. MWP-fit: A program for multiple whole-profile fitting of diffraction peak profiles by ab initio theoretical functions. *Journal of Applied Crystallography* 34 (5), 669–676.
- Romeo, I., Capote, R., Lunar, R., 2007. Crystallographic preferred orientations and microstructure of a Variscan marble mylonite in the Ossa-Morena Zone (SW Iberia). *Journal of structural geology* 29 (8), 1353–1368.
- Rybacki, E., Evans, B., Janssen, C., Wirth, R., Dresen, G., 2013. Influence of stress, temperature, and strain on calcite twins constrained by deformation experiments. *Tectonophysics* 601, 20–36.
- Schaebitz, M., Wirth, R., Janssen, C., Dresen, G., 2015. First evidence of CaCO₃-III and CaCO₃-IIIb high-pressure polymorphs of calcite: Authigenically formed in near surface sediments. *American Mineralogist* 100 (5-6), 1230–1235.
- Schell, N., King, A., Beckmann, F., Fischer, T., Müller, M., Schreyer, A., 2014. The high energy materials science beamline (HEMS) at PETRA III. *Materials Science Forum* 772, 57–61.
- Schmid, S., Panozzo, R., Bauer, S., 1987. Simple shear experiments on calcite rocks: rheology and microfabric. *Journal of structural Geology* 9 (5-6), 747–778.
- Spieckermann, F. C., 2010. Investigation of deformation induced changes of the microstructure of semicrystalline polymers and their impact on mechanical properties. Ph.D. thesis, University of Vienna.
- Turner, F., Griggs, D., Heard, H., 1954. Experimental Deformation of Calcite Crystals. *Geological Society of America Bulletin* 65 (9), 883–&.
- Ungár, T., 2005. Correlation between subgrains and coherently scattering domains. *Powder Diffraction* 20, 366.
- Ungár, T., Glavicic, M., Balogh, L., Nyilas, K., Salem, A., Ribárik, G., Semiatin, S., 2008. The use of X-ray diffraction to determine slip and twinning activity in commercial-purity (CP) titanium. *Materials Science and Engineering: A* 493 (1), 79–85.
- Ungár, T., 1999. The dislocation-based model of strain broadening in X-ray line profile analysis. In: Robert Snyder, Jaroslav Fiala, H. J. B. (Ed.), *Defect and Microstructure Analysis by Diffraction*. Oxford science publications, p. 165–199.
- Ungár, T., Oct. 2004. Microstructural parameters from X-ray diffraction peak broadening. *Scripta Materialia* 51 (8), 777–781.
- Ungár, T., Gubicza, J., Ribárik, G., Borbély, A., 2001. Crystallite size distribution and dislocation structure determined by diffraction profile analysis: principles and practical application to cubic and hexagonal crystals. *Journal of Applied Crystallography* 34 (3), 298–310.
- van der Pluijm, B. A., 1991. Marble mylonites in the Bancroft shear zone, Ontario, Canada: microstruc-

- tures and deformation mechanisms. *Journal of Structural Geology* 13 (10), 1125–1135.
- Vorhauer, A., Pippan, R., Nov. 2004. On the homogeneity of deformation by high pressure torsion. *Scripta Materialia* 51 (9), 921–925.
- Vrijmoed, J. C., Podladchikov, Y. Y., Andersen, T. B., Hartz, E. H., 2009. An alternative model for ultra-high pressure in the Svartberget Fe-Ti garnet-peridotite, Western Gneiss Region, Norway. *European Journal of Mineralogy* 21 (6), 1119–1133.
- Warren, B. E., Averbach, B. L., 1952. The Separation of Cold-Work Distortion and Particle Size Broadening in X-Ray Pattern. *Journal of Applied Physics* 23 (4), 497–497.
- Warren, C., 2013. Exhumation of (ultra-) high-pressure terranes: concepts and mechanisms. *Solid Earth* 4 (1), 75.
- Wilkins, M., 1970. The determination of density and distribution of dislocations in deformed single crystals from broadened X-ray diffraction profiles. *physica status solidi (a)* 2 (2), 359–370.
- Williamson, G., Hall, W., 1953. X-ray line broadening from filed aluminium and wolfram. *Acta Metallurgica* 1 (1), 22 – 31.
- Wojdyr, M., Oct 2010. *Fityk*: a general-purpose peak fitting program. *Journal of Applied Crystallography* 43 (5 Part 1), 1126–1128.
- Zehetbauer, M., Stüwe, H., Vorhauer, A., Schafler, E., Kohout, J., May 2003. The Role of Hydrostatic Pressure in Severe Plastic Deformation. *Advanced Engineering Materials* 5 (5), 330–337.
- Zehetbauer, M. J., Steiner, G., Schafler, E., Korznikov, A. V., Korznikova, E., 2006. Deformation Induced Vacancies with Severe Plastic Deformation: Measurements and Modelling. *Materials Science Forum* 503-504, 57–64.
- Zhilyaev, A. P., Langdon, T. G., Aug. 2008. Using high-pressure torsion for metal processing: Fundamentals and applications. *Progress in Materials Science* 53 (6), 893–979.